Chemical Science

ROYAL SOCIETY OF CHEMISTRY

EDGE ARTICLE

View Article Online
View Journal | View Issue

Cite this: *Chem. Sci.*, 2023, **14**, 6890

All publication charges for this article have been paid for by the Royal Society of Chemistry

Received 4th April 2023
Accepted 5th June 2023

DOI: 10.1039/d3sc01737k

rsc.li/chemical-science

Activation of the cGAS-STING pathway by a mitochondrial DNA-targeted emissive rhodium(III) metallointercalator†

Yue Zheng, ‡ Xiao-Xiao Chen,‡ Dong-Yang Zhang, Wen-Jin Wang, Kun Peng, Zhi-Yuan Li, Zong-Wan Mao * and Cai-Ping Tan *

The cyclic GMP-AMP synthase (cGAS)-stimulator of interferon (STING) pathway is a key mediator of innate immunity involved in cancer development and treatment. The roles of mitochondrial DNA (mtDNA) in cancer immunotherapy have gradually emerged. Herein, we report a highly emissive rhodium(III) complex (**Rh-Mito**) as the mtDNA intercalator. **Rh-Mito** can specifically bind to mtDNA to cause the cytoplasmic release of mtDNA fragments to activate the cGAS-STING pathway. Moreover, **Rh-Mito** activates the mitochondrial retrograde signaling by disturbing the key metabolites involved in epigenetic modifications, which alters the nuclear genome methylation landscape to influence the expression of genes related to immune signaling pathways. Finally, we demonstrate that ferritin-encapsulated **Rh-Mito** elicits potent anticancer activities and evokes intense immune responses *in vivo* by intravenous injection. Overall, we report for the first time that small molecules targeting mtDNA can activate the cGAS-STING pathway, which gives insights into the development of biomacromolecule-targeted immunotherapeutic agents.

1 Introduction

As an important innate immune signal pathway, cyclic GMP-AMP synthase (cGAS)-stimulator of interferon genes (STING) provides great potential for cancer immunotherapy.[1–3] Upon sensing of cytoplasmic DNA, cGAS is activated to catalyse the formation of 2′-3′-cyclic GMP-AMP (cGAMP).[4,5] The activation of STING by cGAMP recruits and activates tank-binding kinase 1 (TBK1), leading to the phosphorylation of interferon regulatory factor 3 (IRF3).[5,6] The phosphorylated IRF3 forms a dimer and reacts with nuclear factor-κB (NF-κB) for nuclear translocation, which induces the expression of type-I interferon (IFN-I) and various inflammatory factors.[7]

At present, most STING activators are synthetic cyclic dinucleotides (CDNs). In 2015, Corrales *et al.* reported that CDN can bind to STING, thereby activating antigen-presenting cells (APCs) and $CD8^+$ T cells.[8] However, CDN-based STING agonists suffer from low metabolic stability, and they need to be administered by intratumoral injection. Several CDN analogues have entered clinical trials, but usually they require combined treatment with immune checkpoint inhibitors (ICIs).[9] Non-nucleotide STING agonists have also attracted much attention due to their high specificity and effectiveness.[2] In 2018, Ramanjulu *et al.* reported that amidobenzimidazole derivatives can act as STING agonists.[10] Lairson's group identified a non-nucleotide cGAMP mimetic SR-717 that can promote the activation of $CD8^+$ T, natural killer and dendritic cells (DCs).[11] Pan *et al.* developed a STING agonist MSA-2 amenable to oral administration.[12] These non-CDN agonists provide possibilities for systemic administration, but the clinical data need further validation. Recently, Jiang's group demonstrated that manganese can promote the activation of the cGAS-STING pathway, and it shows synergistic antitumor immune effects with anti-PD-1 antibody.[13] At the same time, delivery by nanomaterials also provides potential solutions for the *in vivo* applications of STING agonists.[14–22]

The discovery of other activators of the STING pathway has also shown potency in its immunopharmacological regulation.[2] Mitochondria lie at the heart of immunity as they can regulate cancer immune responses from many aspects.[23,24] The importance of mitochondrial retrograde signalling in cancer pathology has been gradually revealed, but its roles in cancer treatment are still unclear.[25–27] Key intermediates in the Krebs cycle such as succinate, fumarate and citrate, are related to immunity and inflammation.[28,29] Mitochondrial DNA (mtDNA) also acts as a danger-associated molecular pattern (DAMP) phagocytosed by DCs to release interferon (IFN) and activate effector T cells, *e.g.*, cytotoxic T lymphocytes (CTLs).[30–32]

MOE Key Laboratory of Bioinorganic and Synthetic Chemistry, School of Chemistry, State Key Laboratory of Oncology in South China, Sun Yat-Sen University, Guangzhou 510006, P. R. China. E-mail: cesmzw@mail.sysu.edu.cn; tancaip@mail.sysu.edu.cn

† Electronic supplementary information (ESI) available. See DOI: https://doi.org/10.1039/d3sc01737k

‡ These authors contributed equally to this work.

Meanwhile, fragmentation of mtDNA can activate the cGAS-STING pathway, which releases NF-κB-dependent transcription of cytokines to recruit $CD8^+$ T cells.[24]

Besides platinum-based anticancer agents, non-platinum metallo-anticancer agents have drawn increasing attention, especially phosphorescent octahedral Ir(III), Ru(II), and Re(I) complexes.[33–35] These complexes are characterized by their multiple functionalities due to the rich photophysical properties, *e.g.*, high quantum yields, long-lived lifetimes, large Stokes shifts and good photostability.[33] Based on the action mechanisms of platinum-based antitumor drugs, rhodium complexes are also considered to be potent anticancer candidates with high biological activities.[33,36–38] Interestingly, kinetically inert rhodium complexes can specifically bind with mismatched DNA and attenuate protein–protein interaction by ligand tuning, and some rhodium complexes exhibit low nanomolar antitumor activity equivalent to or even better than ruthenium/iridium complexes.[37–41]

Considering these research backgrounds, we propose that specific mtDNA-intercalating agents may activate the cGAS-STING pathway for cancer immunotherapy. Moreover, the instinct luminescent properties of rhodium(III) complexes can be used to confirm their mtDNA-targeting specificity. Herein, we report an emissive mtDNA-targeted rhodium(III) complex (**Rh-Mito**) with antiproliferative activity *in vitro*. **Rh-Mito** can induce mtDNA damage to cause the cytoplasmic release of mtDNA fragments for activation of the cGAS-STING signaling pathway, which leads to the maturation of DCs for recruitment of CTLs to the tumor site *in vivo* (Scheme 1). Moreover, by adopting a multi-omics approach, we demonstrate that **Rh-Mito** disturbs mitochondrial metabolites especially those involved in DNA methylation, which alters the nuclear DNA methylation landscape and affects immune gene expression. In all, we present here the first mtDNA intercalator that activates the cGAS-STING pathway, which gives new insights into biomacromolecule-targeted chemo-immunotherapeutic agents.

2 Results

2.1 DNA binding properties *in vitro* and *in situ*

To investigate the structure–activity relationship, **Rh1**,[42] **Rh2**, **Rh3** (ref. 43), and **Rh-Mito** were synthesised by refluxing the dimer precursor with ligands 1,10-phenanthroline (phen), pyrazino[2,3-*f*][1,10]phenanthroline (dpq), dipyrido[3,2-*a*:2′,3′-*c*]phenazine (dppz) and benzo[*i*]dipyrido[3,2-*a*:2′,3′-*c*]phenazine (dppn) in CH_2Cl_2/CH_3OH and purified by silica column chromatography (Scheme S1†). These compounds were characterized by ESI-MS, ^1H NMR, ^{13}C NMR (Fig. S1–S12†) and elemental analysis. The absorption spectra of rhodium(III) complexes are characterized by an intense band at 250–330 nm and a less intense band at 340–500 nm in CH_3CN, CH_2Cl_2 and PBS (Fig. 1A and S13†), which can be attributed to intra-ligand charge transfer (ILCT) and metal-to-ligand charge transfer (MLCT), respectively.[38,41,43] Upon excitation, only **Rh-Mito** displays solvent-dependent red emission with a maximum emission wavelength at 597–654 nm, indicating the imaging potential of **Rh-Mito** (Fig. 1A). The emission quantum yields and lifetimes of **Rh-Mito** fall between 0.07–1.07% and 4.61–8.37 ns, respectively (Table S1†). All of these rhodium(III) complexes show high stability in fetal bovine serum within 24 h according to the monitoring of the UV/Vis spectrum (Fig. S14†). UV/Vis spectroscopy measurement shows that the absorbance of the Rh(III) complexes is proportional to concentration up to 100 μM, indicating their sufficient solubility at working concentrations (Fig. S15†).[44]

The UV/Vis spectrum of **Rh1–Rh3** and **Rh-Mito** exhibits hypochromism in the ILCT band and hyperchromism in the MLCT band upon the addition of calf thymus-DNA (CT-DNA) (Fig. 1B and S16†), and the binding constant (K_b) is calculated to be 5.97×10^6 M^{-1} for **Rh-Mito**, which is much higher than that for reference complexes (**Rh1**: 2.59×10^4 M^{-1}; **Rh2**: 5.20×10^4 M^{-1}; **Rh3**: 5.13×10^5 M^{-1}). Meanwhile, an obvious fluorescence enhancement along with a blue shift of the maximum

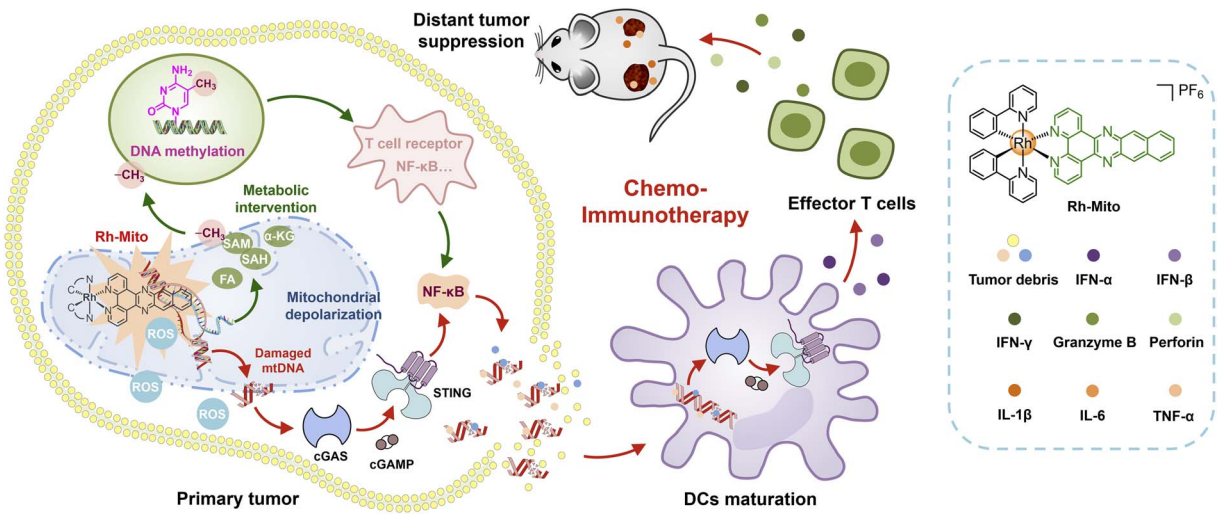

Scheme 1 Schematic illustration of the mechanisms of chemo-immunotherapeutic responses evoked by **Rh-Mito**. SAM: *S*-adenosylmethionine, SAH: *S*-adenosyl homocysteine, FA: fumaric acid, α-KG: α-ketoglutarate, ROS: reactive oxygen species.

emission wavelength is observed for **Rh-Mito** upon the addition of CT-DNA (Fig. S17†). When the molar ratio of [DNA] : [**Rh-Mito**] reaches 8 : 1, the fluorescence of **Rh-Mito** is enhanced by about 2.7 times. In the presence of **Rh-Mito**, the viscosity of CT-DNA increases in a concentration-dependent manner, which proves that it interacts with DNA by intercalation (Fig. 1C). Molecular docking studies using a double-stranded DNA (PDB: 5IP8) show that the dppn ligand in **Rh-Mito** creates a complete intercalation cavity at the terminal C1C2/G9G10 step of duplex, affording a large π-overlap with nucleotide bases (Fig. 1D), and the binding energies are calculated to be −10.90 kcal mol^{-1} for **Δ-Rh-Mito** and −11.03 kcal mol^{-1} for **Λ-Rh-Mito**, which is higher than those obtained for reference complexes (**Rh1**: −7.34 kcal mol^{-1}; **Rh2**: −8.99 kcal mol^{-1}; **Rh3**: −9.90 kcal mol^{-1}; Fig. S18†). These results indicate that the larger planar ligand in rhodium complexes provides higher DNA intercalating capabilities.

Inductively coupled plasma mass spectrometry (ICP-MS) measurement in human cervical cancer (HeLa) cells indicates that the contents of rhodium in mitochondria are much higher than those obtained in cytosol and nuclei after Rh(III) treatment, and the mitochondrial-accumulating ability of **Rh-Mito** is higher than that of **Rh1–Rh3** (Fig. 1E and S19†). Confocal microscopic observations show that the emission of **Rh-Mito** is well overlapped with that of MitoTracker Deep Red (MTDR, Fig. 1F). Moreover, gel electrophoresis analysis of proteins purified from HeLa cells shows minimal interaction of **Rh-Mito** with cellular proteins (Fig. S20†). These results collectively indicate that **Rh-Mito** can specifically bind to mtDNA in cells by the cascade targeting strategy.[45]

2.2 High capabilities to inhibit cancer cell proliferation and stemness

Lipophilicity ($\log P_{o/w}$, in which $P_{o/w}$ = octanol/water partition coefficient) can affect the anticancer mechanisms of metal complexes.[46] As estimated, the $\log P_{o/w}$ values are in the following order: **Rh-Mito** (2.54) > **Rh3** (2.01) > **Rh2** (1.99) > **Rh1** (1.44), which positively correlates with the area of planar ligands. Cellular uptakes of these rhodium(III) complexes were investigated by ICP-MS in HeLa, human lung cancer (A549), human breast cancer (MCF-7), human liver cancer (HepG2) and human normal breast (MCF-10A) cells (Table S2†). The uptake capability of **Rh-Mito** is basically stronger than that of **Rh1–Rh3**. As expected, the uptake efficiency of **Rh-Mito** in cancer cells is also much higher than that in normal cells. After being incubated at 4 °C or pretreated with metabolic inhibitor carbonyl cyanide *m*-chlorophenyl hydrazone (CCCP),[47] cellular rhodium contents are obviously decreased (Table S3†), and the pretreatment of the endocytosis inhibitor chloroquine doesn't show obvious influence on its cellular uptake level, which indicated that **Rh-Mito** penetrates into HeLa cells through energy-dependent active transportation.

The *in vitro* antiproliferative activities of **Rh1–Rh3** and **Rh-Mito** were further assessed on HeLa, human breast cancer

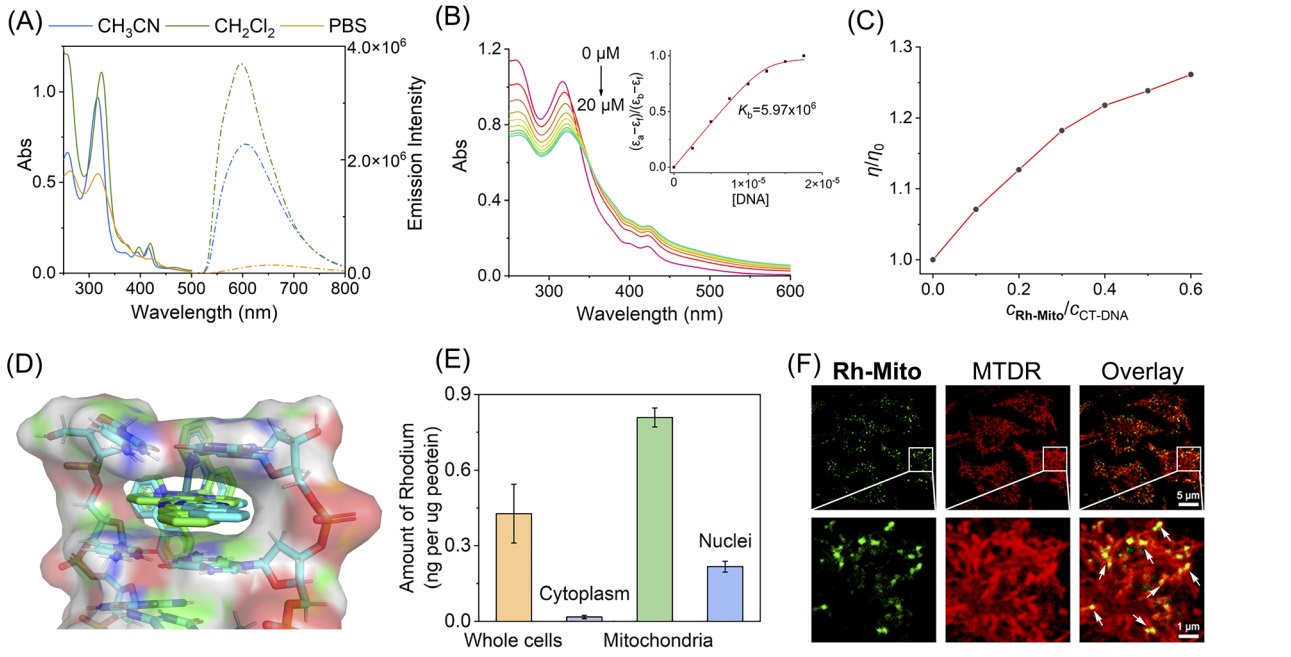

Fig. 1 (A) UV/Vis spectra and emission spectra of **Rh-Mito** (10 μM) measured in degassed CH_3CN, CH_2Cl_2 and PBS at 298 K. (B) UV/Vis spectra of **Rh-Mito** (10 μM) titrated with CT-DNA (0–20 μM) in Tris–HCl buffer. The arrow shows the alteration in the absorption intensity of **Rh-Mito** upon the addition of CT-DNA. Insert: Plot of $(\varepsilon_a - \varepsilon_f)/(\varepsilon_b - \varepsilon_f)$ against [DNA] for the binding of **Rh-Mito** to CT-DNA. (C) Effect of **Rh-Mito** and **Rh-Mito** on the relative viscosity of CT-DNA. (D) Molecular docking studies of **Δ-Rh-Mito** (green) and **Λ-Rh-Mito** (cyan) with double-stranded DNA (PDB: 5IP8). The DNA fragment is shown in colors as a cartoon representation. (E) Distribution of **Rh-Mito** (1.0 μM, 1 h) in cellular compartments of HeLa cells measured by ICP-MS. (F) Colocalization of **Rh-Mito** with MTDR analysed by confocal microscopy. The lower pictures are the enlarged parts of the red boxes in the upper pictures. **Rh-Mito**: λ_{ex} = 405 nm; λ_{em} = 620 ± 20 nm. MTDR: λ_{ex} = 633 nm; λ_{em} = 660 ± 20 nm. For (E) and (F), the cell viability is proved to be over 95% by MTT assay under the experimental conditions.

Table 1 Antiproliferative activity (IC_{50} values) of **Rh-Mito** and CDDP against different cell lines[a]

	IC_{50} (μM)								
Complexes	HeLa	HeLa-ρ0 (MTFs)	MCF-7	MB-MDA-231	A549	NCI-H1299	HepG2	MCF-10A	HLF
Rh-Mito	0.4 ± 0.1	2.7 ± 0.2 (6.7)	0.6 ± 0.1	0.8 ± 0.1	0.5 ± 0.1	0.4 ± 0.1	1.9 ± 0.2	3.2 ± 0.3	4.7 ± 0.4
CDDP	7.9 ± 0.6	7.1 ± 0.7 (0.9)	8.6 ± 1.5	13.9 ± 2.1	10.2 ± 0.9	12.4 ± 1.9	12.9 ± 1.4	12.8 ± 1.6	8.4 ± 0.9

[a] Data are presented as the mean ± standard deviation (SD), and antiproliferative activity was assessed after 72 h of incubation.

(MCF-7 and MDA-MB-231), human lung cancer (A549 and NCI-H1299), HepG2, MCF-10A and human lung fibroblast (HLF) cells. **Rh-Mito** exhibits low IC_{50} values ranging from 0.4 to 1.9 μM in cancer cells and relatively high IC_{50} values (3.2–4.7 μM) in normal cells, and the antiproliferative activity of **Rh-Mito** is about 7–31 times that of cisplatin in cancer cells (CDDP, Table 1). The IC_{50} values of **Rh-Mito** are also higher than that of **Rh1**–**Rh3** in most cancer cells, which is consistent with their uptake efficacies (Table S4†). Trypan Blue assay[48,49] also shows that **Rh-Mito** can successfully reduce the cell viability, and the 50% cytotoxicity concentration (CC_{50}) values against the tested cell lines fall between 0.5 and 3.3 μM (Table S5†).

The mtDNA-targeting factor (MTF) defined as the ratios of the IC_{50} value in HeLa-ρ0 (mtDNA-less HeLa) cells to that in wild-type HeLa cells calculated for **Rh-Mito** is about 6.7, higher than that for the other complexes (**Rh1**: 0.8; **Rh2**: 2.3; **Rh3**: 5.7), which indicates that mtDNA damage caused by **Rh-Mito** plays an indispensable role in its antiproliferative capability. In the non-toxic nanomolar concentrations, **Rh-Mito** can inhibit the colony formation of HeLa cells in a concentration-dependent manner (Fig. S21†), which confirms its effectiveness in reducing cancer cell proliferation and stemness.

2.3 MtDNA damage-induced mitochondrial dysfunction and necroptosis

Rh-Mito causes an obviously enhanced immunofluorescent signal of 8-oxoguanine (8-OG; the most common form of oxidative in DNA)[50] mainly in the cytoplasm (Fig. 2A). Compared with that of nuclear DNA (nucDNA), the copy number of mtDNA is decreased by about 75% after **Rh-Mito** treatment at 2.0 μM (Fig. 2B; Table S6†). Moreover, **Rh-Mito** treatment reduces the amplification of mtDNA segments significantly and its impact on nucDNA is unobvious (Fig. 2C). Gel electrophoresis shows that **Rh-Mito** treatment causes obvious fragmentation of mtDNA in HeLa cells (Fig. 2D).

Human mitochondrial genome encodes 37 genes, of which 13 genes are essential components of the oxidative phosphorylation (OXPHOS) system.[51] Real-time quantitative polymerase chain reaction (RT-qPCR) shows that the expression of ND1, ND3, ND4, ND5 COX2, ATP6 and ATP8 is decreased in HeLa cells treated with **Rh-Mito** (fold change > 2, Fig. 2E). These genes encode subunits of nicotinamide adenine dinucleotide (NADH) dehydrogenase, cytochrome c oxidase and ATP synthase belonging to the complexes of the respiratory chain complex.[52] Consistently, rhodamine 123 (Rh123) staining shows that **Rh-Mito** can decrease the mitochondrial membrane potential (MMP) in a time-dependent manner (Fig. 2F). In cells treated with **Rh-Mito** (2.0 μM, 6 h), the intracellular ATP level is also notably suppressed by about 83% (Fig. 2G).

The impact of **Rh-Mito** on mitochondrial respiration and glycolysis was then evaluated by measuring the oxygen consumption rate (OCR, Fig. 2H) and extracellular acidification rate (ECAR, Fig. 2I), respectively. **Rh-Mito** induces a dose-dependent decrease in basal respiration, ATP production, maximum respiration and non-mitochondrial respiration (Fig. S22†), along with a dose-dependent inhibition of glycolysis, glycolytic reserve and glycolytic capacity (Fig. S23†). These results suggest that **Rh-Mito** can suppress the transcription of mtDNA and impair mitochondrial functions.

The expression of Bcl-2 is decreased upon **Rh-Mito** treatment, accompanied by an increased expression in Bax, resulting in a decreased Bcl-2/Bax ratio (Fig. 2J). The expression of the guardian of genome p53 is increased, and the cleavage of two regulatory proteins of apoptosis, caspase-3 and -9, is also detected. Accordingly, **Rh-Mito** induces a dose-dependent increase in the proportion of cells in the late apoptosis/necrosis phase (Fig. 2K). Moreover, pretreatment of z-VAD-fmk (50 μM; a pan-caspase inhibitor) and Necrostatin-1 (50 μM; an inhibitor of receptor-interacting protein 1 regulating programmed necrosis) diminishes the antiproliferative activity of **Rh-Mito** (Fig. S24†), while minimal effects are detected for the other cell death inhibitors tested. These results suggest that **Rh-Mito** induces necroptosis through a mitochondrial-mediated pathway by damaging mtDNA.

2.4 cGAS-STING pathway activation in both HeLa cells and DCs

Since **Rh-Mito** can damage mtDNA, we next evaluated whether **Rh-Mito** can elevate mitochondrial ROS levels and cause cytoplasmic DNA release. 2′,7′-Dichlorodihydrofluorescein diacetate (H_2DCFDA) staining shows that **Rh-Mito** treatment markedly elevates mitochondrial ROS, as the punctate fluorescence of DCF well colocalizes with that of MTDR (Fig. 3A). After **Rh-Mito** treatment, the fluorescence of PicoGreen gradually separates from that of MTDR, indicating the cytoplasmic release of mtDNA, while MTDR and PicoGreen show a well colocalization pattern in the control cells. Moreover, giant and bright nucleoids (green spots) are formed in **Rh-Mito**-treated HeLa cells after 1 h treatment, indicating the remodeling of mitochondrial nucleoids as a result of mtDNA damage. Finally, the mitochondrial morphology changes from tightly connected filaments to loosely dispersion dots, accompanied by the gradually

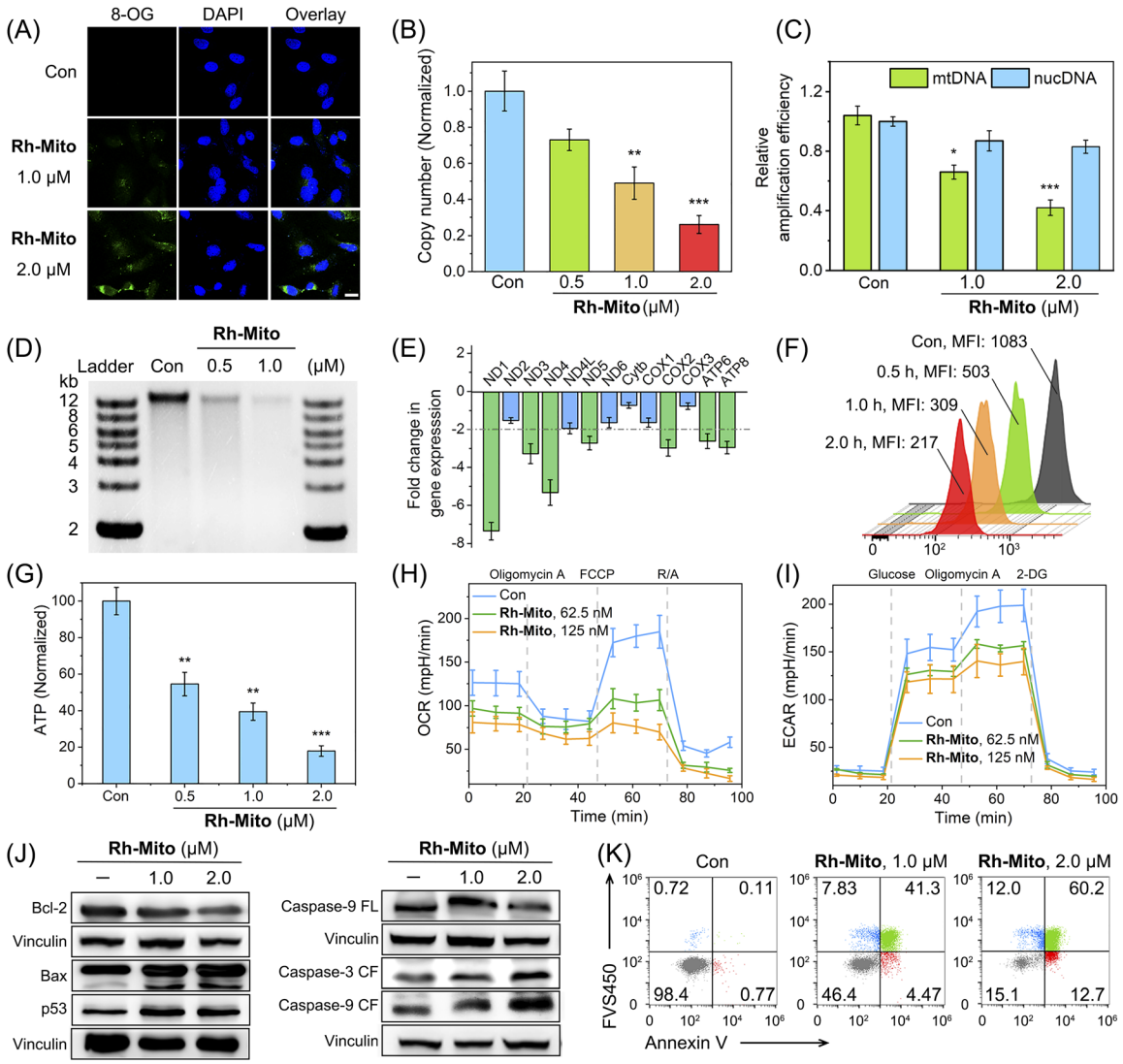

Fig. 2 (A) Immunofluorescence staining of 8-OG in HeLa cells treated with **Rh-Mito** at the indicated concentrations for 6 h. 8-OG: $\lambda_{ex} = 488$ nm; $\lambda_{em} = 518 \pm 20$ nm. 4′,6-Diamidino-2-phenylindole dihydrochloride (DAPI): $\lambda_{ex} = 405$ nm; $\lambda_{em} = 461 \pm 20$ nm. Scale bar: 10 μm. (B and C) Impact of **Rh-Mito** on mtDNA copy number and amplification. HeLa cells were treated with **Rh-Mito** for 6 h. (D) Gel electrophoresis showing mtDNA damage in HeLa cells incubated with **Rh-Mito** for 2 h. (E) Impact of **Rh-Mito** (1.0 μM, 6 h) on the expression of 13 genes encoded by the mitochondrial genome. (F) Impact of **Rh-Mito** (1.0 μM) on MMP by Rh123 staining. $\lambda_{ex} = 488$ nm, $\lambda_{em} = 530 \pm 20$ nm. (G) Impact of **Rh-Mito** (6 h) on the intracellular ATP levels. OCR (H) and ECAR (I) profiles of HeLa cells treated with **Rh-Mito** for 2 h. R/A: a mixture of rotenone and antimycin A. 2-DG: 2-deoxyglucose. (J) Western blotting analysis of the effects of **Rh-Mito** on the expression of the proteins. HeLa cells were treated with **Rh-Mito** for 6 h. FL: full length. CF: cleaved form. Vinculin was used as the internal reference. (K) Annexin V-APC and FVS450-BV421 double staining of HeLa cells treated with **Rh-Mito** for 12 h. Annexin V-APC: $\lambda_{ex} = 637$ nm, $\lambda_{em} = 670 \pm 20$ nm. FVS450-BV421: $\lambda_{ex} = 405$ nm, $\lambda_{em} = 440 \pm 20$ nm. *$p < 0.05$, **$p < 0.01$ and ***$p < 0.001$ by the Student's two-tailed t test.

disappeared fluorescence of PicoGreen, which implies that mitochondria are damaged and mtDNA is degraded gradually (Fig. 3B).

The cGAS-STING pathway activates NF-κB to induce cytokines to promote cell death, which further leads to the release of DNA fragments as tumor-derived antigens.[3] Uptake of DNA fragments by DCs elicits a complimentary cGAS-STING-dependent type I IFN-mediated antitumor immune response.[53] The content of cGAMP upon **Rh-Mito** treatments is significantly increased in a dose-dependent manner in HeLa cells (Fig. 3C), along with elevated expression levels of cGAS and p-STING (Fig. 3E). Similar phenomena are found in DCs incubated with the supernate from **Rh-Mito**-treated HeLa cells (Fig. 3D and F). As expected, the phosphorylation of IKKβ and IκB-α is markedly increased in HeLa cells upon **Rh-Mito** treatment (Fig. 3G), which indicates that **Rh-Mito** causes the elevation of cGAMP leading to activation of STING and its downstream factor NF-κB.

2.5 Mitochondrial metabolism and key epigenetic metabolite dysregulation

As mitochondrial bioenergetics and cancer metabolism are closely connected, we then measured the impact of **Rh-Mito** on

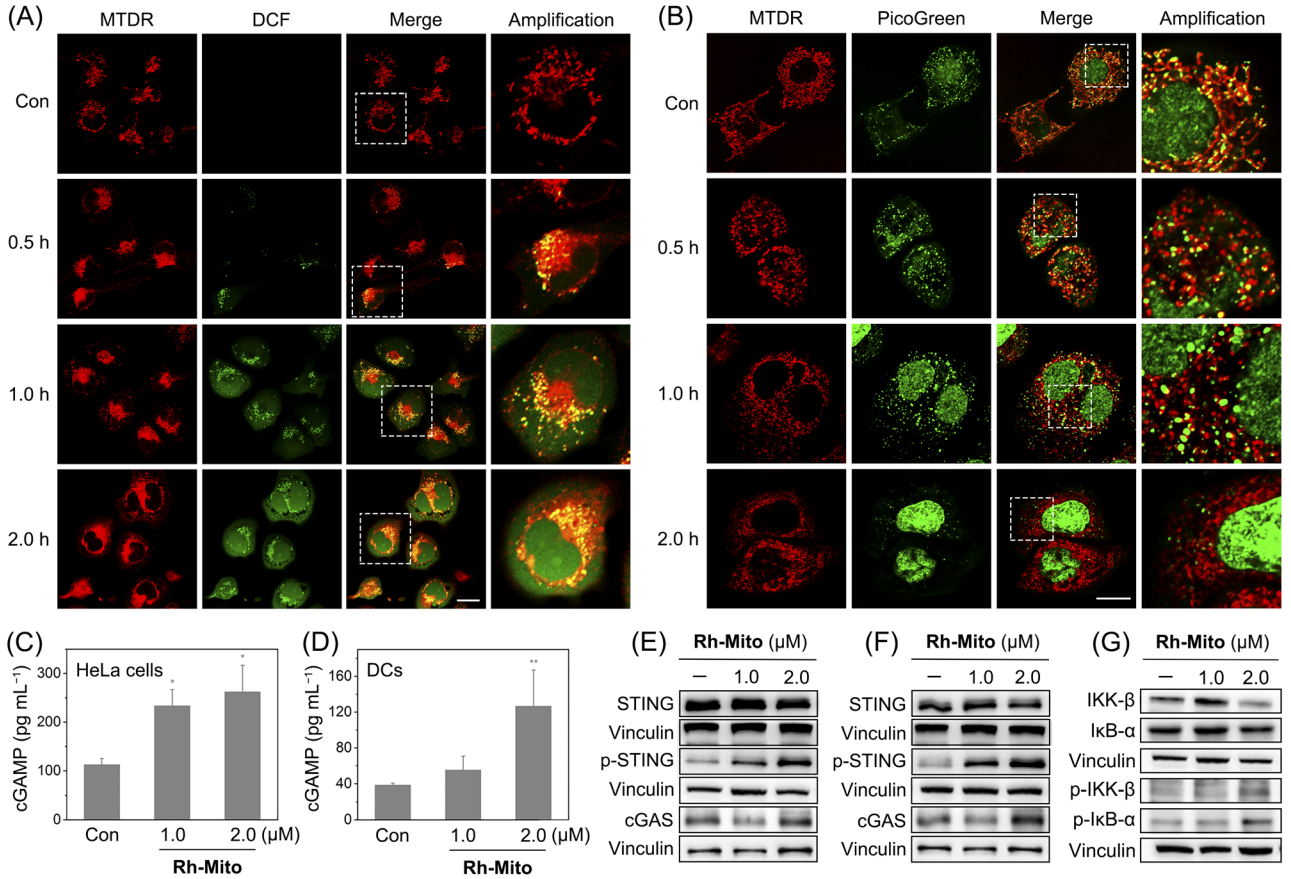

Fig. 3 Confocal images of HeLa cells double-labeled with H_2DCFDA/MTDR (A) or PicoGreen/MTDR (B). HeLa cells were treated with **Rh-Mito** (0.5 μM) for different time intervals. Con: control. DCF: $\lambda_{ex} = 488$ nm; $\lambda_{em} = 520 \pm 20$ nm. MTDR: $\lambda_{ex} = 633$ nm; $\lambda_{em} = 660 \pm 20$ nm. PicoGreen: $\lambda_{ex} = 488$ nm; $\lambda_{em} = 525 \pm 20$ nm. The images in the right column are the magnified views of those in the left boxes. Scale bar: 10 μm. The impact of **Rh-Mito** treatment on cGAMP levels in HeLa cells (C) and DCs (D) measured by ELISA. The impact of **Rh-Mito** treatment (6 h) on the expression of proteins measured by western blotting in HeLa cells (E) and DCs (F). For (D) and (F), DCs were cultured with the supernate of **Rh-Mito**-treated HeLa cells for 6 h. (G) The impact of **Rh-Mito** treatment (6 h) on the phosphorylation of IKK and IκB-α in HeLa cells. *$p < 0.05$, **$p < 0.01$ and ***$p < 0.001$ by the Student's two-tailed *t* test.

cancer cell metabolism by gas chromatography-time of-flight mass spectrometry (GC-TOF-MS). The data were analyzed by principal component analysis (PCA) to find outliers (Fig. S25†). Orthogonal partial least squares discriminant analysis (OPLS-DA) score plots show a distinct metabolic profile for **Rh-Mito**-treated samples compared with the control (Fig. S26†). Based on a criterion of VIP > 1 and $p < 0.05$, 715 (up-regulated: 55; down-regulated: 660) and 299 (up-regulated: 102; down-regulated: 197) differential metabolites are detected for the positive and negative ion modes in **Rh-Mito**-treated samples, respectively (Fig. S27 and ESI Data S1 and S2†). These biomarkers are selected and further analyzed with MetaboAnalyst to investigate the potential metabolic pathways (Fig. 4A and S28†). **Rh-Mito** treatment influences several metabolic pathways including alanine, aspartate and glutamate metabolism, pyrimidine metabolism, purine metabolism, pentose phosphate and tricarboxylic acid (TCA) pathways. As a mtDNA intercalator, **Rh-Mito** strongly disturbs the nucleic acid-related metabolic pathways, including the content of bases (adenine, uracil and cytosine; Fig. 4B) and nucleosides (guanosine, cytidine, thymidine and uridine, Fig. 4C).

Interestingly, several metabolites in one-carbon metabolism and the TCA cycle involved in epigenetic modifications are influenced by **Rh-Mito** treatment. DNA demethylation reactions utilize α-kG as the cofactor, while FA acts as the inhibitor of these reactions.[54] SAM is the methyl group donor for DNA methyltransferases, while SAH is the reaction product and a competitive inhibitor of them (Fig. S29†).[55] After treatment with **Rh-Mito**, α-kG (*ca.* 6.54-fold), fumaric acid (*ca.* 2.67-fold), L-serine (*ca.* 2.12-fold), methionine (*ca.* 2.77-fold) and SAH (*ca.* 1.69-fold) are down-regulated (Fig. 4D and E). A concentration-dependent increase in the ratio of SAM/SAH is detected by enzyme-linked immunosorbent assay (ELISA, Fig. 4F). The SAM/SAH ratio increases by about 12-fold in HeLa cells treated with **Rh-Mito** (2.0 μM, 6 h). These results indicate that **Rh-Mito** can influence cancer metabolome and may alter the epigenetic methylation status.

2.6 DNA-methylated status alteration and immuno-pathway regulation

As **Rh-Mito** affects the intracellular metabolites related to methylation (SAM/SAH) and demethylation (α-kG) reactions, we first investigated its impact on DNA methylation levels by dot

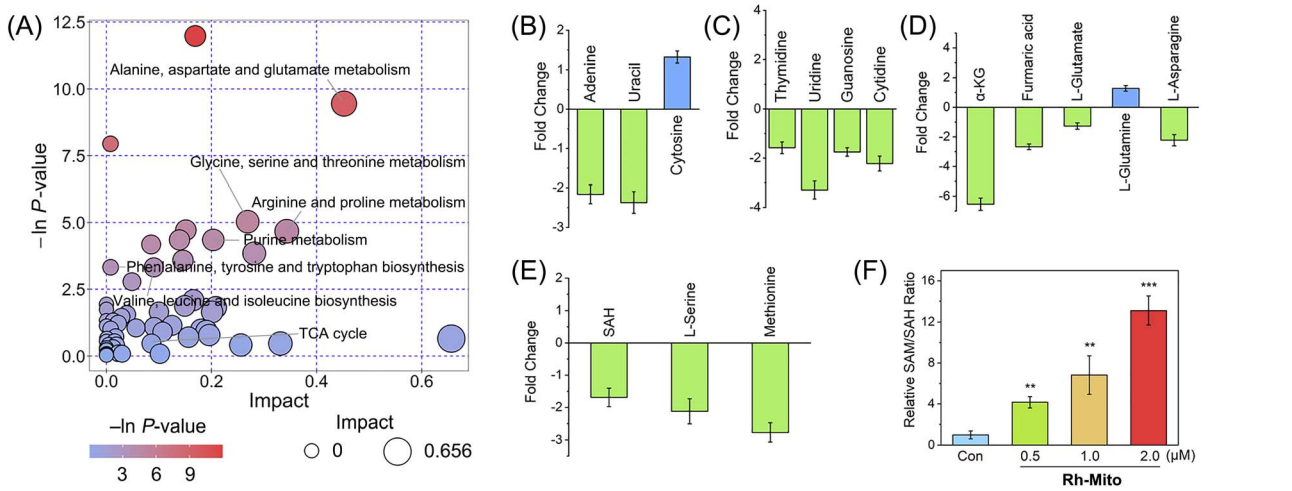

Fig. 4 (A) Alternations in the metabolic pathways in HeLa cells treated with **Rh-Mito** (1.0 μM, 6 h). These metabolites are analysed by GC-TOF-MS in the positive mode. The color of the circles means the *p*-value, and the area of the circles means pathway impact. The impact of **Rh-Mito** treatment on the cellular levels of base metabolites (B), nucleoside metabolites (C), TCA cycle and glutaminolysis-related metabolites (D), and one-carbon metabolism-related metabolites (E). The relative content is normalized by the peak area of adonitol (internal standard). (F) The impact of **Rh-Mito** (6 h) on the SAM/SAH ratio detected with ELISA. $*p < 0.05$, $**p < 0.01$ and $***p < 0.001$ by the Student's two-tailed *t* test.

blotting. **Rh-Mito** treatment causes an obvious increase in 5-methylcytosine (5mC) in wild-type HeLa cells (Fig. 5A) but makes it invariantly in mtDNA-free HeLa-ρ0 cell (Fig. S30†). Accordingly, as the demethylated product, 5-hydroxymethylcytosine (5hmC) is markedly decreased by **Rh-Mito** treatment (Fig. S31†), which is consistent with the variation trend of α-kG.

The impact of **Rh-Mito** on 5mC methylation at the genomic level was further analyzed by reduced representation bisulphite sequencing (RRBS) and the number of methylated C sites in different sequence contexts (CG, CHH, CHG, where H represents A, C, T) was counted. The methylated status in the CG sequence context where most of the methylated C sites locate (>98.9%) was dominantly analyzed (Fig. S32†). The cancer genome always shows hypomethylation generally but hypermethylation of CpG islands in the promoter region of tumor suppressor genes.[56] The genome methylation status is different in various biological samples, and differentially methylated regions (DMRs) are thought to be involved in the regulation of the gene transcription level.[57] 1537 hypermethylated DMRs (hyper-DMRs) and 6022 hypomethylated DMRs (hypo-DMRs) are screened out in HeLa cells (Fig. 5B and ESI Data S3†). After being treated with **Rh-Mito**, the average methylated level in hyper-DMR is decreased, while the hypo-DMR level is increased. Gene Ontology (GO) analysis shows that DMR-related gene categories including the nucleus, metabolic process and DNA binding and transcription are significantly influenced by **Rh-Mito** treatment (Fig. S33†). Consistent with the previous results, Kyoto Encyclopedia of Genes and Genomes (KEGG) enrichment analysis shows that **Rh-Mito** mainly influences signaling pathways closely associated with mitochondrial metabolism, cancer progression and immunity including metabolic, cGMP, cAMP, Ras-associated protein-1 (Rap1) and mitogen-activated protein kinase (MAPK) signaling pathways (Fig. 5C).

DNA methylation plays pivotal roles in gene transcription,; we then use RNA-sequencing (RNA-Seq) to study the impact of **Rh-Mito** on the transcriptome. The correlation coefficients between every two individual samples from the same group are above 0.97 (Fig. S34A†), implying the reproducibility of the experiment. The overall Q30 percentage is above 93.6%. More than 94.1% of readings are mapped to reference genes in all samples, and 78.3% of readings are located in exons (Fig. S34B†). The expression levels of 742 and 347 genes are found to be up-regulated and down-regulated, respectively (Fig. 5D and ESI Data S4†). The heatmap of RNA-Seq shows that expression patterns are very similar across each treatment group (Fig. S35†). GO analysis shows that **Rh-Mito** causes significant overall changes in gene categories including the nucleus, DNA binding and transcription (Fig. S36†). The KEGG pathway annotation indicates that various pathways involved in cancer for immunity and progression including p53, NF-κB, T cell receptor, Toll-like receptor (TLR) and anus kinase/signal transducers and activators of transcription (JAK/STAT) signaling pathway are influenced by **Rh-Mito** treatment (Fig. 5E). Gene set enrichment analysis (GSEA) shows that alternation of genes expression is negatively related to mitochondria-associated metabolism (Fig. 5F and S37A†) and positively related to apoptosis and immune signaling pathways (Fig. 5G and S37B†).

Finally, we correlated the result of methylome with transcriptome to screen out those differentially expressed genes (DEGs) with DMRs induced by **Rh-Mito** treatment. Generally, the gene expression level is negatively correlated with the DNA methylated level in promoter and gene body regions (Fig. S38†). The correlation between DEGs and DMRs in promoter regions is much higher than that in gene body regions (Fig. S39†). Therefore, these DEGs with DMRs in promoter regions are investigated, as shown in Fig. 5H and ESI Data S5.† Among

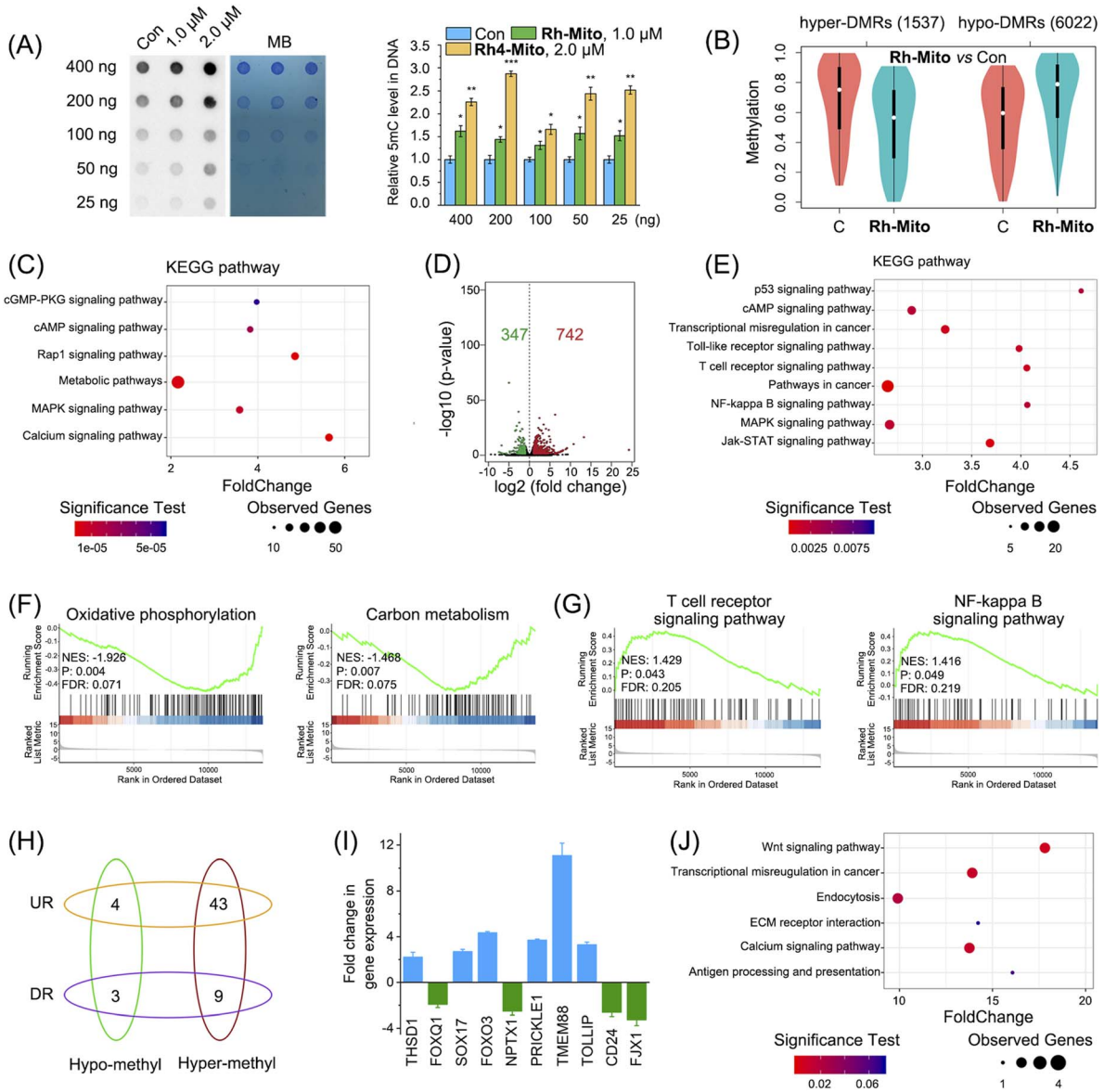

Fig. 5 (A) The impact of **Rh-Mito** (6 h) on the 5mC levels determined by dot blotting assay. Methylene blue (MB) represents the loading control of DNA samples. (B) Average methylated levels in DMRs between the control and **Rh-Mito**-treated HeLa cells (1.0 μM, 6 h). (C) KEGG enrichment analysis shows pathways influenced by **Rh-Mito** treatment (1.0 μM, 6 h) in RRBS. (D) Volcano plots showing the DEGs in HeLa cells treated with **Rh-Mito** (1.0 μM, 6 h). Standard: p-value < 0.05; VIP > 1; fold change > 2. (E) KEGG enrichment analysis of pathways influenced by **Rh-Mito** treatment (1.0 μM, 6 h). (F and G) GSEA reveals negative and positive enrichment of **Rh-Mito**-altered genes in various cellular processes. NES: normalized enrichment score. FDR: false-positive rate. (H) Overlapping of DEGs with DMRs. UR: up-regulated genes, DR: down-regulated genes. (I) Validation of DEGs regulated by DMRs related to oncogenes or immunomodulators using RT-qPCR. Relative fold changes in gene expression were normalized according to the average expression of the housekeeping gene β-actin. (J) KEGG enrichment analysis was performed to identify pathways mediated by **Rh-Mito** treatment (1.0 μM, 6 h) in anchoring promoter regions. *p < 0.05, **p < 0.01 and ***p < 0.001 by the Student's two-tailed t test.

them, the expression of oncogenes and immune modulators including THSD1, FOXQ1, SOX17, FOXO3, NPTX1, PRICKLE1, TMEM88, TOLLIP, CD24, and FJX1 is influenced by **Rh-Mito** treatment (Table S7†), which is further validated by RT-qPCR (Fig. 5I). GO analysis shows that **Rh-Mito** causes significant overall changes in gene categories including the nucleus, DNA binding and transcription (Fig. S40†). The KEGG pathway annotation indicates that various pathways involved in cancer development and immunity including antigen presentation are influenced by **Rh-Mito** (Fig. 5J). These results suggest that **Rh-Mito** can affect the signaling pathways related to cancer growth and immunity by regulating the DNA methylation status.

2.7 cGAS-STING pathway activation to evoke antitumor immunity *in vivo*

Finally, an immunocompetent cervical cancer subcutaneous bearing mouse model was established to evaluate the antitumor

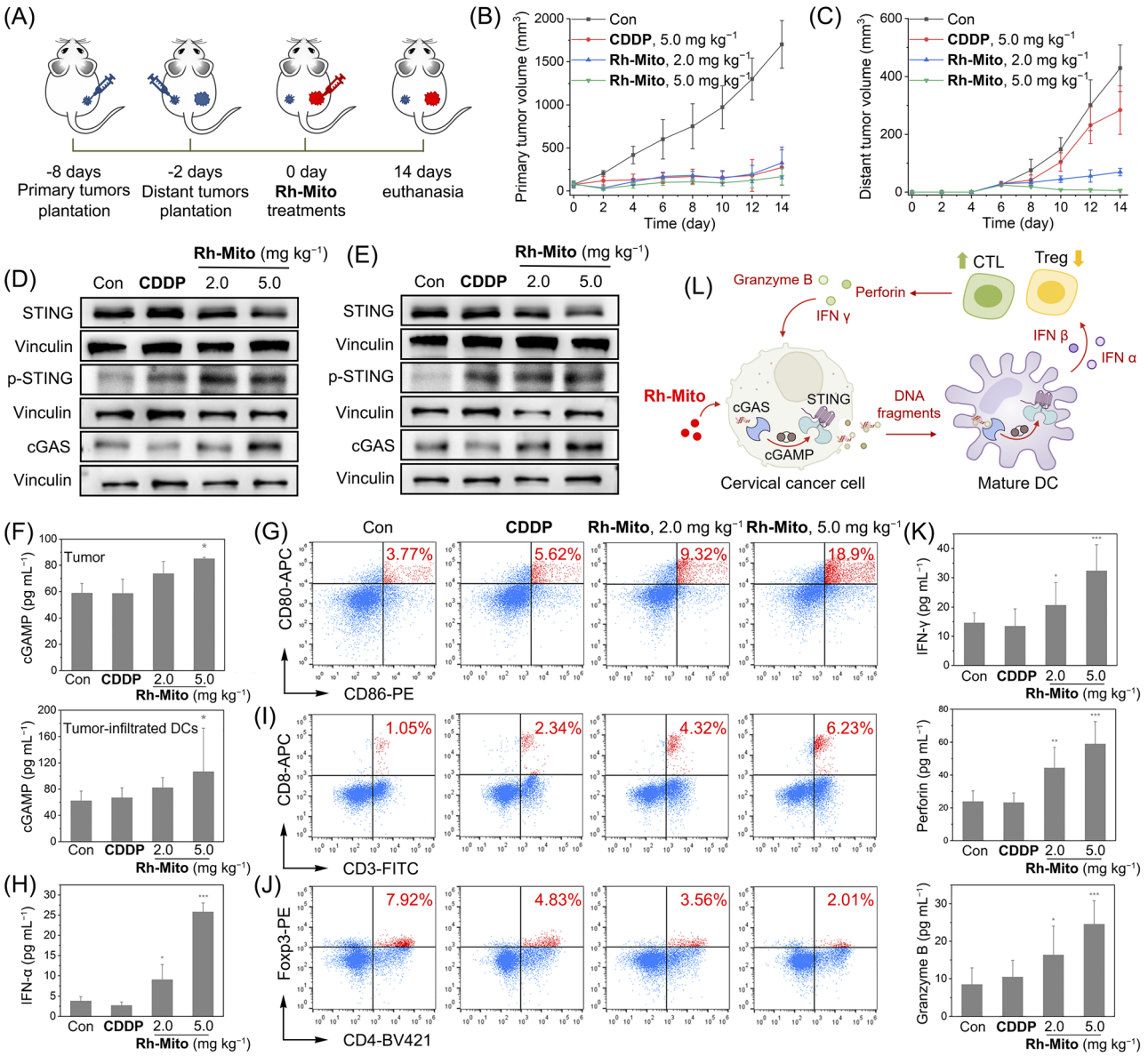

Fig. 6 (A) Schematic illustration of the *in vivo* therapeutic protocol. (B and C) The volume curves of primary tumors (B) and distant tumors. (D–F) Western blots showing elevated expression of cGAS and p-STING in tumor (D) and tumor-infiltrated DCs (E). (F and H) ELISA showing increased cGAMP in tumor and tumor-infiltrated DCs (F), and type I IFNs (IFN-α) in serum (H). Quantitative detection of populations of $CD86^+CD80^+$ DCs (gating on $CD11c^+$, G), $CD8^+$ (I) and $Foxp3^+$ T cells (J) in tumors after different treatments ($n = 3$). (K) Secretion of IFN-γ, perforin and granzyme B in serum measured by ELISA assay ($n = 3$). (L) Schematic illustration of the modulation of anticancer immunity by **Rh-Mito** *in vivo*. *$p < 0.05$, **$p < 0.01$ and ***$p < 0.001$ by the Student's two-tailed *t* test.

potency of **Rh-Mito** *in vivo*. Mouse cervical cancer (U14) cells were inoculated to the BALB/c mice as primary tumors. 6 days later, U14 cells were planted into the contralateral as distant tumors (Fig. 6A). **Rh-Mito** was intratumorally injected into the primary tumors and the tumor volumes were monitored for 14 days. At the end of the treatment, no significant weight change (Fig. S41†) nor organ damage of mice is found (Fig. S42†). The growth of both the primary and distant tumors is successfully inhibited upon **Rh-Mito** treatment (Fig. 6B and C and S43†). The *in vivo* inhibitory effects of **Rh-Mito** are better than those of CDDP, especially for distant tumors.

Compared with the control mice, the cGAMP content as well as the expression levels of cGAS and *p*-STING levels are markedly elevated in the **Rh-Mito**-treated group in both tumor and tumor-infiltrated DCs (Fig. 6D–F). The proportion of $CD86^+CD80^+$ cells, hallmarks for DC maturation, also increases from about 3.77% to 18.9% in mice treated with **Rh-Mito** at the higher dose (Fig. 6G). Both IFN-α and IFN-β in serum are elevated after **Rh-Mito** treatment (Fig. 6H and S44†). Accordingly, the percentage of CTLs ($CD8^+$ T cells) in the tumor section of **Rh-Mito**-treated samples increases from about 1.05% to 6.23% (Fig. 6I), and $CD4^+$ T cells are also increased from about 13.7% to 32.0% (Fig. S45†). Moreover, the regulatory T cells

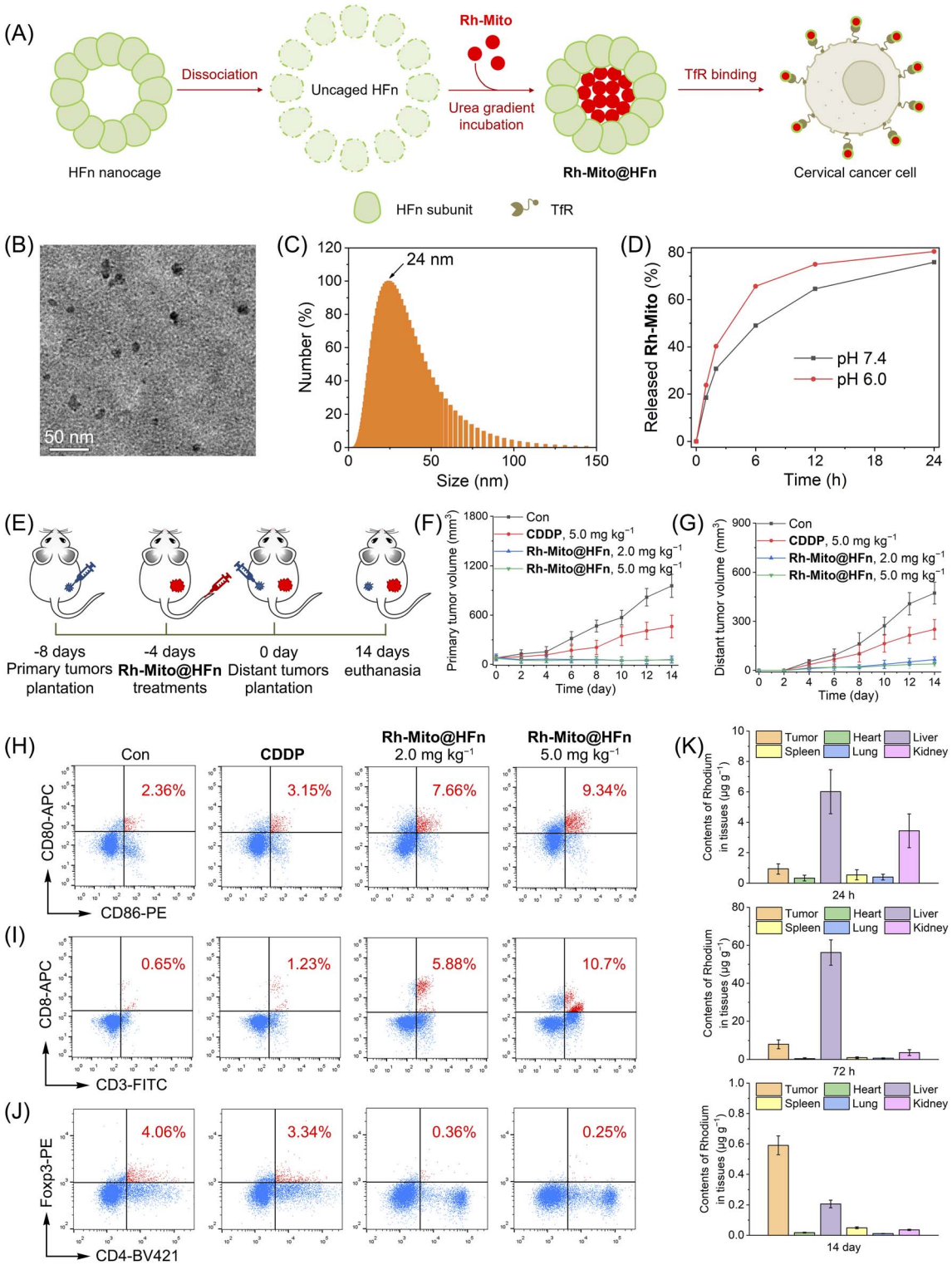

Fig. 7 (A) The construction of **Rh-Mito@HFn** NPs. (B) The TEM image of **Rh-Mito@HFn** NPs. (C) Size distribution of **Rh-Mito@HFn** NPs characterized by DLS. (D) Time-dependent release of **Rh-Mito** from **Rh-Mito@HFn** NPs in buffer with different pH values. (E) Schematic illustration of *in vivo* therapeutic protocol. The volume curves of primary tumors (F) and distant tumors (G) upon different treatments. Quantitative detection of populations of $CD86^+CD80^+$ DCs (H, gating on $CD11c^+$), $CD8^+$ (I), and $Foxp3^+$ T cells (J) in tumors after different treatment ($n = 3$) by flow cytometry. (K) Contents of rhodium in diverse organs of tumor-bearing mice at different time points.

($Foxp3^+$ T cells) are decreased from 7.92% to 2.01% (Fig. 6J). CTLs can release IFN-γ, perforin and granzyme B to directly kill tumor cells, and all of these secreta are increased upon **Rh-Mito** treatments (Fig. 6K). Finally, obvious increases in pro-inflammatory cytokines (interleukin (IL)-1β, IL-6, and tumor necrosis factor-α (TNF-α)) in serum are also detected (Fig. S46†).

These results show that **Rh-Mito** can activate the CTLs and regulatory T cells, cause the maturation of DCs, and improve the cancer immune microenvironments by activating the cGAS-STING pathway *in vivo* (Fig. 6L).

In order to improve the solubility and bioavailability of **Rh-Mito**, we use the recombination of human heavy-chain ferritin (HFn) to deliver it for intravenous injection (Fig. 7A). Ferritin is an iron storage protein comprising 24 subunits that can assemble into a spherical cage for the encapsulation of drugs.[58] HFn can bind to transferrin receptor 1 (TfR1) overexpressing in many cancer types so as to achieve tumor-targeted delivery.[59] Transmission electron microscope (TEM) observation shows that **Rh-Mito@HFn** nanoparticles (NPs) display a pseudo spherical nanostructure with an average diameter of 10.5 nm (Fig. 7B). Dynamic light scattering (DLS) measurement shows that the average hydrodynamic diameter of **Rh-Mito@HFn** NPs is about 24.0 nm with a narrow distribution pattern (Fig. 7C). The release rates of **Rh-Mito** from **Rh-Mito@HFn** NPs are about 63% and 75% at pH 6.0 and 7.4 after 12 h, respectively (Fig. 7D). Confocal microscopic observation shows that **Rh-Mito@HFn** NPs first localize in lysosomes in HeLa cells after 1 h incubation, and the emission of **Rh-Mito** displays a high colocalization with MTDR after 4 h (Fig. S47†), which indicates that **Rh-Mito** can be successfully released and retain its mtDNA targeting properties.

The antitumor efficacy of **Rh-Mito@HFn** NPs was evaluated on U14 cancer and the therapeutic protocol is illustrated in Fig. 7E. U14 cells were inoculated to the BALB/c mice as primary tumors. 4 days later, **Rh-Mito@HFn** NPs were intravenously injected. After another 4 days, U14 cells were planted into the contralateral as distant tumors. After 14 days of treatment, the inhibitory rates of **Rh-Mito@HFn** NPs on primary and distant tumors are about 95.4% and 86.1%, respectively (Fig. 7F and G and S48†). **Rh-Mito@HFn** NP treatment increases the content of $CD86^+CD80^+$ cells from about 2.36% to 9.34%, which indicates that it can increase the maturation of DCs (Fig. 7H). Moreover, **Rh-Mito@HFn** NPs increase the percentage of CTLs ($CD8^+$ T cells) from about 0.65% to 10.7% (Fig. 7I) and downregulate the regulatory T cells ($Foxp3^+$ T) cells from about 4.06% to 0.25% (Fig. 7J). The $CD4^+$ T cells are also increased from 6.19% to 31.9% (Fig. S49†).

The content of Rh in different organs was measured by ICP-MS to investigate the distribution and metabolism of **Rh-Mito@HFn** NPs (Fig. 7K). At 24 h and 72 h post-injection, Rh mainly concentrates in the liver, kidney and tumor, which indicates that **Rh-Mito@HFn** NPs possess good tumor-targeting properties. On day 14, the Rh content in all organs, including tumor tissue, was very low ($<0.6\ \mu g\ g^{-1}$), which proves that **Rh-Mito@HFn** NPs can be metabolized in the body. Moreover, **Rh-Mito@HFn** NPs did not cause body weight loss in mice at the end of the treatment (Fig. S50†).

3 Discussion

The cGAS-STING pathway plays important roles in the innate immune responses triggered by viruses, bacteria, parasite infections as well as cancer immunity by regulating protein synthesis and cytokine expression through phosphorylation, ubiquitination and dimerization.[3,60] cGAS-STING can also be activated by sensing endogenous DNA, including extranuclear chromatin and DNA fragments released from mitochondria, which makes it an important regulator in autoimmunity, inflammation and cell senescence.[5,61] The release of damaged mtDNA into cytosol can activate the cGAS-STING pathway, which induces cytokine expression leading to the recruitment and activation of immune cells.[7,32] Traditional therapies, *e.g.*, radiotherapy and chemotherapy, can cause cell death by inducing DNA damage, while they can also activate the cGAS-STING pathway to enhance DC-mediated antigen presentation and T cell response.[62] For example, cisplatin is reported to activate the cGAS/STING axis and enhance the anticancer immune response.[63] Recent studies have shown that STING is a potent target in cancer therapy, and agonists of STING have been developed rapidly.[2,64] Moreover, non-CDN STING agonists, small molecules, and metal ions have also been proven to be effective in activating the STING pathway.[10–13,65] In this study, we report a metal complex **Rh-Mito** with an octahedral three-dimensional structure as the mtDNA intercalating agent. Due to its cationic lipophilic nature, **Rh-Mito** can accumulate in mitochondria to cause mtDNA damage resulting in its cytosolic release, which activates the cGAS-STING pathway.

Recent studies have shown that mitochondrial metabolism is closely related to the epigenetic status of cells.[29] SAM, an intermediate metabolite of one-carbon metabolism, is the most important donor of methylation reactions, while its downstream product SAH can inhibit the activity of methyl transferase.[66] Another important intermediate metabolite of the TCA cycle, α-KG, is a cofactor for histone/DNA/RNA demethylases.[54] Furthermore, epigenetic modifications play key roles in immunogenic activation, tumor antigen presentation, T-cell infiltration, and tumor immunosuppression.[67–70] Most solid tumors show loss of overall methylation and hypermethylation of CpG island in the tumor suppressor gene promoter region, which silences antitumor immunity genes and impairs antigen recognition and presentation.[71] In this work, we find that **Rh-Mito** can interfere with cellular metabolic pathways by damaging mtDNA, especially nucleotide anabolism, and metabolites related to DNA methylation modifications. Combined with the results of RRBS and RNA-seq, we show that **Rh-Mito** can affect the 5mC DNA modification to regulate the immune pathways, including the cGAS-STING pathway. The regulation of cancer immunity through epigenetic modifications caused by attenuation in mitochondrial metabolome reflects the importance of mitochondrial retrograde signaling in shaping the immune microenvironments. We propose that the metabolic modulation may be an effective complement to the cGAS-STING pathway activated by the cytoplasmic release of mtDNA.

The activation of the cGAS-STING signaling pathway is considered to be a very effective strategy for tumor immunotherapy, and the treatment by intratumoral injection of CDNs has shown significant efficacy in preclinical studies and is undergoing human clinical trials.[72] However, CDNs are hydrophilic molecules, and they are not easy to penetrate the membrane. CDNs are also easy to hydrolyze, making them not

feasible for systematic administration.[2] With the development of structural modification strategies and non-CDN agonists, the stability of STING agonists has been improved, but they also face toxicity problems.[2,64] The unsatisfactory initial clinical trial results of STING agonists trigger an urgent need for efficient delivery strategies, including liposomes and inorganic NPs.[14–16] In our work, we use HFn nanocages as the carrier for **Rh-Mito**. We demonstrate that **Rh-Mito@HFn** NPs possess good tumor-targeting capability and high biocompatibility, and they can successfully evoke potent antitumor immune responses by intravenous injection.

4 Conclusion

In summary, we report an mtDNA-targeting rhodium(III) complex, **Rh-Mito**, as an effective cancer immunotherapeutic agent. **Rh-Mito** can damage mtDNA to cause mitochondrial damage and the cytosolic leakage of mtDNA fragments, which elicits the cGAS-STING-dependent type I IFN-mediated antitumor immune responses. Moreover, **Rh-Mito** disturbs the mitochondrial metabolic status and alters several key metabolites involved in epigenetic modification to reshape the nucDNA methylation landscape. Moreover, we also prove that **Rh-Mito** encapsulated in HFn nanocages can activate tumor immunotherapeutic responses *in vivo* by intravenous administration. Overall, we demonstrate that mtDNA-targeted small molecules can activate cGAS-STING signaling, which provides new insight into the design of potential immune-modulating anticancer agents.

Data availability

RNA-sequencing data are deposited and available on the Gene Expression Omnibus under accession ID GSE221227 with secure token ijkncqqexbebvwr (**https://www.ncbi.nlm.nih.gov/geo/**). RRBS data for DNA methylation are deposited and available on Sequence Read Archive under accession ID PRJNA913445 with link **https://dataview.ncbi.nlm.nih.gov/object/PRJNA913445?reviewer=jtm1nu53im54t3vt8oonohbn2p**.

Author contributions

YZ and XXC contributed equally to this work. YZ, ZWM, and CPT conceived this study and designed the experiments. YZ, DYZ, KP, and ZYL completed material synthesis and characterization and analyzed the data. WJW performed the docking assay and analyzed computational data. YZ, DYZ, and XXC carried out cellular studies and analyzed the data. YZ and XXC conducted the *in vivo* studies and analyzed the data. YZ, XXC, ZWM, and CPT analyzed the results and wrote the manuscript. YZ, ZWM, and CPT provided the funds to support this article. All authors revised this manuscript.

Conflicts of interest

There are no conflicts to declare.

Acknowledgements

This study was supported by the National Natural Science Foundation of China (No. 22022707, 22107124, 22177142, 21837006 and 91953117), China Postdoctoral Science Foundation (No. 2021M693604), and the Fundamental Research Funds for the Central Universities.

References

1 G. N. Barber, *Nat. Rev. Immunol.*, 2015, **15**, 760–770.
2 K. M. Garland, T. L. Sheehy and J. T. Wilson, *Chem. Rev.*, 2022, **122**, 5977–6039.
3 J. Kwon and S. F. Bakhoum, *Cancer Discovery*, 2020, **10**, 26–39.
4 X. Cai, Y. H. Chiu and Z. J. Chen, *Mol. Cell*, 2014, **54**, 289–296.
5 K. P. Hopfner and V. Hornung, *Nat. Rev. Mol. Cell Biol.*, 2020, **21**, 501–521.
6 Y. Tanaka and Z. J. Chen, *Sci. Signaling*, 2012, **5**, ra20.
7 A. Decout, J. D. Katz, S. Venkatraman and A. Ablasser, *Nat. Rev. Immunol.*, 2021, **21**, 548–569.
8 L. Corrales, L. H. Glickman, S. M. McWhirter, D. B. Kanne, K. E. Sivick, G. E. Katibah, S. R. Woo, E. Lemmens, T. Banda, J. J. Leong, K. Metchette, T. W. Dubensky Jr and T. F. Gajewski, *Cell Rep.*, 2015, **11**, 1018–1030.
9 K. Luo, N. Li, W. Ye, H. Gao, X. Luo and B. Cheng, *Molecules*, 2022, **27**, 4638.
10 J. M. Ramanjulu, G. S. Pesiridis, J. Yang, N. Concha, R. Singhaus, S. Y. Zhang, J. L. Tran, P. Moore, S. Lehmann, H. C. Eberl, M. Muelbaier, J. L. Schneck, J. Clemens, M. Adam, J. Mehlmann, J. Romano, A. Morales, J. Kang, L. Leister, T. L. Graybill, A. K. Charnley, G. Ye, N. Nevins, K. Behnia, A. I. Wolf, V. Kasparcova, K. Nurse, L. Wang, A. C. Puhl, Y. Li, M. Klein, C. B. Hopson, J. Guss, M. Bantscheff, G. Bergamini, M. A. Reilly, Y. Lian, K. J. Duffy, J. Adams, K. P. Foley, P. J. Gough, R. W. Marquis, J. Smothers, A. Hoos and J. Bertin, *Nature*, 2018, **564**, 439–443.
11 E. N. Chin, C. Yu, V. F. Vartabedian, Y. Jia, M. Kumar, A. M. Gamo, W. Vernier, S. H. Ali, M. Kissai, D. C. Lazar, N. Nguyen, L. E. Pereira, B. Benish, A. K. Woods, S. B. Joseph, A. Chu, K. A. Johnson, P. N. Sander, F. Martínez-Peña, E. N. Hampton, T. S. Young, D. W. Wolan, A. K. Chatterjee, P. G. Schultz, H. Michael Petrassi, J. R. Teijaro and L. L. Lairson, *Science*, 2020, **369**, 993–999.
12 B. S. Pan, S. A. Perera, J. A. Piesvaux, J. P. Presland, G. K. Schroeder, J. N. Cumming, B. W. Trotter, M. D. Altman, A. V. Buevich, B. Cash, S. Cemerski, W. Chang, Y. Chen, P. J. Dandliker, G. Feng, A. Haidle, T. Henderson, J. Jewell, I. Kariv, I. Knemeyer, J. Kopinja, B. M. Lacey, J. Laskey, C. A. Lesburg, R. Liang, B. J. Long, M. Lu, Y. Ma, E. C. Minnihan, G. O'Donnell, R. Otte, L. Price, L. Rakhilina, B. Sauvagnat, S. Sharma, S. Tyagarajan, H. Woo, D. F. Wyss, S. Xu, D. J. Bennett and G. H. Addona, *Science*, 2020, **369**, 935.

13 M. Lv, M. Chen, R. Zhang, W. Zhang, C. Wang, Y. Zhang, X. Wei, Y. Guan, J. Liu, K. Feng, M. Jing, X. Wang, Y. C. Liu, Q. Mei, W. Han and Z. Jiang, *Cell Res.*, 2020, **30**, 966–979.

14 D. Shae, K. W. Becker, P. Christov, D. S. Yun, A. K. R. Lytton-Jean, S. Sevimli, M. Ascano, M. Kelley, D. B. Johnson, J. M. Balko and J. T. Wilson, *Nat. Nanotechnol.*, 2019, **14**, 269–278.

15 X. Sun, Y. Zhang, J. Li, K. S. Park, K. Han, X. Zhou, Y. Xu, J. Nam, J. Xu, X. Shi, L. Wei, Y. L. Lei and J. J. Moon, *Nat. Nanotechnol.*, 2021, **16**, 1260–1270.

16 E. L. Dane, A. Belessiotis-Richards, C. Backlund, J. Wang, K. Hidaka, L. E. Milling, S. Bhagchandani, M. B. Melo, S. Wu, N. Li, N. Donahue, K. Ni, L. Ma, M. Okaniwa, M. M. Stevens, A. Alexander-Katz and D. J. Irvine, *Nat. Mater.*, 2022, **21**, 710–720.

17 X. Lu, L. Miao, W. Gao and Z. Chen, *Sci. Transl. Med.*, 2020, **12**, eaaz6606.

18 F. Wang, H. Su, D. Xu, W. Dai, W. Zhang, Z. Wang, C. F. Anderson, M. Zheng, R. Oh, F. Wan and H. Cui, *Nat. Biomed. Eng.*, 2020, **4**, 1090–1101.

19 Z. Luo, X. Liang, T. He, X. Qin, X. Li, Y. Li, L. Li, X. J. Loh, C. Gong and X. Liu, *J. Am. Chem. Soc.*, 2022, **144**, 16366–16377.

20 T. Luo, G. T. Nash, X. Jiang, X. Feng, J. Mao, J. Liu, A. Juloori, A. T. Pearson and W. Lin, *Adv. Mater.*, 2022, **34**, e2110588.

21 K. Yang, W. Han, X. Jiang, A. Piffko, J. Bugno, C. Han, S. Li, H. Liang, Z. Xu, W. Zheng, L. Wang, J. Wang, X. Huang, J. P. Y. Ting, Y. X. Fu, W. Lin and R. R. Weichselbaum, *Nat. Nanotechnol.*, 2022, **17**, 1322–1331.

22 W. H. Li, J. Y. Su and Y. M. Li, *Acc. Chem. Res.*, 2022, **55**, 2660–2671.

23 E. L. Mills, B. Kelly and L. A. J. O'Neill, *Nat. Immunol.*, 2017, **18**, 488–498.

24 C. R. Harapas, E. Idiiatullina, M. Al-Azab, K. Hrovat-Schaale, T. Reygaerts, A. Steiner, P. Laohamonthonkul, S. Davidson, C. H. Yu, L. Booty and S. L. Masters, *Nat. Rev. Immunol.*, 2022, **22**, 535–549.

25 M. G. Vizioli, T. Liu, K. N. Miller, N. A. Robertson, K. Gilroy, A. B. Lagnado, A. Perez-Garcia, C. Kiourtis, N. Dasgupta, X. Lei, P. J. Kruger, C. Nixon, W. Clark, D. Jurk, T. G. Bird, J. F. Passos, S. L. Berger, Z. Dou and P. D. Adams, *Genes Dev.*, 2020, **34**, 428–445.

26 M. Tigano, D. C. Vargas, S. Tremblay-Belzile, Y. Fu and A. Sfeir, *Nature*, 2021, **591**, 477–481.

27 M. Rigon, A. R. Townley and M. Campanella, *Cell Metab.*, 2021, **33**, 853–855.

28 M. D. Buck, R. T. Sowell, S. M. Kaech and E. L. Pearce, *Cell*, 2017, **169**, 570–586.

29 I. Martinez-Reyes and N. S. Chandel, *Nat. Commun.*, 2020, **11**, 102.

30 L. S. Huang, Z. Hong, W. Wu, S. Xiong, M. Zhong, X. Gao, J. Rehman and A. B. Malik, *Immunity*, 2020, **52**, 475–486.

31 C. H. Yu, S. Davidson, C. R. Harapas, J. B. Hilton, M. J. Mlodzianoski, P. Laohamonthonkul, C. Louis, R. R. J. Low, J. Moecking, D. De Nardo, K. R. Balka, D. J. Calleja, F. Moghaddas, E. Ni, C. A. McLean, A. L. Samson, S. Tyebji, C. J. Tonkin, C. R. Bye, B. J. Turner, G. Pepin, M. P. Gantier, K. L. Rogers, K. McArthur, P. J. Crouch and S. L. Masters, *Cell*, 2020, **183**, 636–649.

32 K. W. Chung, P. Dhillon, S. Huang, X. Sheng, R. Shrestha, C. Qiu, B. A. Kaufman, J. Park, L. Pei, J. Baur, M. Palmer and K. Susztak, *Cell Metab.*, 2019, **30**, 784–799.

33 C. C. Lee Lawrence and K. M. Lo Kenneth, *J. Am. Chem. Soc.*, 2022, **144**, 14420–14440.

34 H. Huang, S. Banerjee, K. Qiu, P. Zhang, O. Blacque, T. Malcomson, M. J. Paterson, G. J. Clarkson, M. Staniforth, V. G. Stavros, G. Gasser, H. Chao and P. J. Sadler, *Nat. Chem.*, 2019, **11**, 1041–1048.

35 Z. Y. Pan, C. P. Tan, L. S. Rao, H. Zhang, Y. Zheng, L. Hao, L. N. Ji and Z. W. Mao, *Angew. Chem., Int. Ed.*, 2020, **59**, 18755–18762.

36 S. Medici, M. Peana, V. M. Nurchi, J. I. Lachowicz, G. Crisponi and M. A. Zoroddu, *Coord. Chem. Rev.*, 2015, **284**, 329–350.

37 K. M. Boyle and J. K. Barton, *J. Am. Chem. Soc.*, 2018, **140**, 5612–5624.

38 D. L. Ma, L. J. Liu, K. H. Leung, Y. T. Chen, H. J. Zhong, D. S. Chan, H. M. Wang and C. H. Leung, *Angew. Chem., Int. Ed.*, 2014, **53**, 9178–9182.

39 A. C. Komor and J. K. Barton, *J. Am. Chem. Soc.*, 2014, **136**, 14160–14172.

40 J. M. Bailis, A. G. Weidmann, N. F. Mariano and J. K. Barton, *PNAS*, 2017, **114**, 6948–6953.

41 G. J. Yang, W. Wang, S. W. F. Mok, C. Wu, B. Y. K. Law, X. M. Miao, K. J. Wu, H. J. Zhong, C. Y. Wong, V. K. W. Wong, D. L. Ma and C. H. Leung, *Angew. Chem., Int. Ed.*, 2018, **57**, 13091–13095.

42 T.-S. Kang, W. Wang, H.-J. Zhong, J.-X. Liang, C.-N. Ko, J.-J. Lu, X.-P. Chen, D.-L. Ma and C.-H. Leung, *Biochim. Biophys. Acta, Gen. Subj.*, 2017, **1861**, 256–263.

43 H. Liang, T. Hao, C. Yin, X. Yang, H. Fu, X. Zheng, R. Li, D. Xiao and H. Chen, *Eur. J. Inorg. Chem.*, 2017, **2017**, 4149–4157.

44 Y.-Y. Ling, Y.-J. Kong, L. Hao, Z.-Y. Pan, Z.-W. Mao and C.-P. Tan, *Inorg. Chem. Front.*, 2023, **10**, 3284–3292.

45 K. Peng, Y. Zheng, W. Xia and Z.-W. Mao, *Chem. Soc. Rev.*, 2023, **52**, 2790–2832.

46 K. K.-W. Lo, B. T.-N. Chan, H.-W. Liu, K. Y. Zhang, S. P.-Y. Li and T. S.-M. Tang, *Chem. Commun.*, 2013, **49**, 4271–4273.

47 Y. Zheng, L. He, D.-Y. Zhang, C.-P. Tan, L.-N. Ji and Z.-W. Mao, *Dalton Trans.*, 2017, **46**, 11395–11407.

48 R. Mirzayans, B. Andrais and D. Murray, *Int. J. Mol. Sci.*, 2017, **18**, 1679.

49 A. Eastman, *Oncotarget*, 2017, **8**, 8854–8866.

50 X. Cheng, C. Kelso, V. Hornak, C. d. l. Santos, A. P. Grollman and C. Simmerling, *J. Am. Chem. Soc.*, 2005, **127**, 13906–13918.

51 E. A. Schon, S. DiMauro and M. Hirano, *Nat. Rev. Genet.*, 2012, **13**, 878–890.

52 C. Yan, X. Duanmu, L. Zeng, B. Liu and Z. Song, *Cells*, 2019, **8**, 379.

53 M. Motwani, S. Pesiridis and K. A. Fitzgerald, *Nat. Rev. Genet.*, 2019, **20**, 657–674.
54 M. Xiao, H. Yang, W. Xu, S. Ma, H. Lin, H. Zhu, L. Liu, Y. Liu, C. Yang, Y. Xu, S. Zhao, D. Ye, Y. Xiong and K. L. Guan, *Genes Dev.*, 2012, **26**, 1326–1338.
55 M. Yang and K. H. Vousden, *Nat. Rev. Cancer*, 2016, **16**, 650–662.
56 Z. D. Smith and A. Meissner, *Nat. Rev. Genet.*, 2013, **14**, 204–220.
57 F. Song, J. F. Smith, M. T. Kimura, A. D. Morrow, T. Matsuyama, H. Nagase and W. A. Held, *PNAS*, 2005, **102**, 3336–3341.
58 N. Song, J. Zhang, J. Zhai, J. Hong, C. Yuan and M. Liang, *Acc. Chem. Res.*, 2021, **54**, 3313–3325.
59 K. Fan, C. Cao, Y. Pan, D. Lu, D. Yang, J. Feng, L. Song, M. Liang and X. Yan, *Nat. Nanotechnol.*, 2012, **7**, 459–464.
60 X. Zhang, X. C. Bai and Z. J. Chen, *Immunity*, 2020, **53**, 43–53.
61 K. N. Miller, S. G. Victorelli, H. Salmonowicz, N. Dasgupta, T. Liu, J. F. Passos and P. D. Adams, *Cell*, 2021, **184**, 5506–5526.
62 S. Yum, M. Li and Z. J. Chen, *Cell Res.*, 2020, **30**, 639–648.
63 S. Grabosch, M. Bulatovic, F. Zeng, T. Ma, L. Zhang, M. Ross, J. Brozick, Y. Fang, G. Tseng, E. Kim, A. Gambotto, E. Elishaev, R. P. Edwards and A. M. Vlad, *Oncogene*, 2019, **38**, 2380–2393.
64 Q. Zhang, C. Chen, B. Xia and P. Xu, *Curr. Opin. Chem. Biol.*, 2022, **69**, 102170.
65 D. Lu, G. Shang, J. Li, Y. Lu, X. C. Bai and X. Zhang, *Nature*, 2022, **604**, 557–562.
66 J. W. Locasale, *Nat. Rev. Cancer*, 2013, **13**, 572–583.
67 E. Dai, Z. Zhu, S. Wahed, Z. Qu, W. J. Storkus and Z. S. Guo, *Mol. Cancer*, 2021, **20**, 171.
68 Z. Zhou, K. Van der Jeught, Y. Fang, T. Yu, Y. Li, Z. Ao, S. Liu, L. Zhang, Y. Yang, H. Eyvani, M. L. Cox, X. Wang, X. He, G. Ji, B. P. Schneider, F. Guo, J. Wan, X. Zhang and X. Lu, *Nat. Biomed. Eng.*, 2021, **5**, 1320–1335.
69 Q. Duan, H. Zhang, J. Zheng and L. Zhang, *Trends Cancer*, 2020, **6**, 605–618.
70 W. Sheng, M. W. LaFleur, T. H. Nguyen, S. Chen, A. Chakravarthy, J. R. Conway, Y. Li, H. Chen, H. Yang, P. H. Hsu, E. M. Van Allen, G. J. Freeman, D. D. De Carvalho, H. H. He, A. H. Sharpe and Y. Shi, *Cell*, 2018, **174**, 549–563.
71 X. Pan and L. Zheng, *Cell. Mol. Immunol.*, 2020, **17**, 940–953.
72 A. Guilherme, L. A. Rowland, H. Wang and M. P. Czech, *Trends Cell Biol.*, 2023, **33**, 340–354.